Chemical Science

EDGE ARTICLE

View Article Online
View Journal | View Issue

Cite this: *Chem. Sci.*, 2019, **10**, 3779

All publication charges for this article have been paid for by the Royal Society of Chemistry

Functional black phosphorus nanosheets for mitochondria-targeting photothermal/photodynamic synergistic cancer therapy†

Xiaoyan Yang,[a] Dongya Wang,[a] Jiawei Zhu,[a] Lei Xue,[a] Changjin Ou,[a] Wenjun Wang,[b] Min Lu,*[a] Xuejiao Song*[a] and Xiaochen Dong *[a]

Received 30th October 2018
Accepted 13th February 2019

DOI: 10.1039/c8sc04844d

rsc.li/chemical-science

Organelle-targeting nanosystems are envisioned as promising tools for phototherapy, which can generate heat or reactive oxygen species (ROS) induced cytotoxicity in the targeted location but leave the surrounding biological tissues undamaged. In this work, an imaging-guided mitochondria-targeting photothermal/photodynamic nanosystem has been developed on the basis of functionalized black phosphorus (BP) nanosheets (NSs). In the nanosystem, BP NSs are coated with polydopamine (PDA) and then covalently linked with both chlorin e6 (Ce6) and triphenyl phosphonium (TPP) through carbodiimide reaction between the amino group and the carboxyl group, forming BP@PDA–Ce6&TPP NSs. Due to the strong absorbance of BP@PDA in the near-infrared region and the highly efficient ROS generation of Ce6, the as-prepared nanosystem with mitochondria-targeting capacity (TPP moiety) shows remarkably enhanced efficiency in cancer cell killing. Combined photothermal and photodynamic therapy is implemented and monitored by *in vivo* fluorescence imaging, achieving excellent performance in inhibiting tumor growth. This study presents a novel nanotheranostic agent for mitochondria-targeting phototherapy, which may open new horizons for biomedicine.

Introduction

Nanomaterial based organelle-targeting phototherapy is considered as a promising route for desired cancer theranostics on account of its distinct advantages, including minimal invasiveness, improved selectivity, high therapeutic efficiency, mitigated side effects and low complications.[1,2] Typically, nanomaterial based phototherapy consists of photothermal therapy (PTT) and photodynamic therapy (PDT). PTT, using photo-absorbing agents, can transform light energy into heat to cause cell death.[3,4] PDT utilizes photosensitizers (PSs) to generate reactive oxygen species (ROS) under light irradiation, which causes oxidative stress and membrane damage and finally kills cancer cells.[5] Unfortunately, till now, single modal phototherapy still faces many difficulties in destroying tumors due to some challenges, such as the intrinsic depth-dependent decline of photon density, inhomogeneous local hyperthermia in PTT,[6] and hypoxic tumor microenvironment in PDT.[7] Alternatively, the combination of PTT and PDT can be an approach to overcome these challenges. In addition, it was found that mild photothermal heating (*e.g.* at ~43 °C) could promote the cellular uptake of drugs or photosensitizers.[8] It is believed that the development of organelle-targeting synergistic PTT/PDT nanosystems is promising to win the battle against cancer, achieving desirable therapeutic effects with minimized systemic side effects.[9,10]

Currently, nanomaterials for phototherapy can be divided into three types: organic,[11–14] inorganic,[1] and organic–inorganic hybridized nanomaterials.[15] Traditional organic nanomaterials possess high biocompatibility and low toxicity, but photobleaching and low thermal stability have hindered their biomedical applications. Meanwhile, inorganic nanomaterials have been widely investigated due to their easy modification, tunable morphology, and desirable physiological stability. For example, a variety of inorganic nanomaterials, including graphene and its derivatives,[16,17] noble-metal nanomaterials,[18] transition metal carbide or carbon nitride (MXene),[19,20] transition metal dichalcogenides (TMDs),[21,22] boron nitride (BN),[23] metal–organic frameworks,[24] and graphitic carbon nitride (g-C_3N_4),[25] have been demonstrated as potential candidates for phototherapy. However, concerns about the safety and biocompatibility of these nanomaterials still persist.

Fortunately, since 2015, black phosphorus (BP) based nanomaterials have emerged as a new type of inorganic material for biomedicine due to their biocompatibility, biodegradability, and biosafety (the metabolism of BP would not cause

[a]Key Laboratory of Flexible Electronics (KLOFE), Institute of Advanced Materials (IAM), School of Physical and Mathematical Science, Nanjing Tech University (NanjingTech), 30 South Puzhu Road, Nanjing 211800, China. E-mail: iamxcdong@njtech.edu.cn; iammlv@njtech.edu.cn; songxuejiao8888@163.com

[b]School of Physical Science and Information Technology, Liaocheng University, Liaocheng 252059, China

† Electronic supplementary information (ESI) available: Experimental methods and additional figures. See DOI: 10.1039/c8sc04844d

certain immune responses).[26,27] For instance, BP nanomaterials have been used as photothermal agents owing to their negligible cytotoxicity and distinguishing cancer therapeutic efficacy due to their broad NIR absorption.[28,29] Particularly, the unique layer-dependent energy band makes ultrathin BP nanosheets (NSs) efficient photosensitizers for ROS generation.[30] Furthermore, BP NSs with a corrugated plane configuration possess large surface area and thus can act as a delivery system for drugs,[31] magnetic nanoparticles,[32] targeting molecules,[33,34] and photosensitizers,[35] forming synergistic therapeutic systems.

Despite the recent advances in BP based therapeutic systems, there is still plenty of room for improving the therapeutic effects of BP based nanosystems. For example, common BP based nanosystems rely on physical interactions with other materials to form therapeutic systems, which suffer from undesired release and might be harmful to healthy tissues.[31,33] Considering that covalent functionalization can overcome this issue, we herein prepare both chlorin e6 (Ce6) and triphenyl phosphonium (TPP) covalently functionalized BP NSs for fluorescence and thermal imaging guided mitochondria-targeting synergistic PTT/PDT (Fig. 1). Dopamine (DA) is a small-molecule mimic of the adhesive proteins of mussels due to the catechol and amine groups. It can self-polymerize under alkaline conditions to generate polydopamine (PDA) layer atop virtually any surface with strong binding affinity.[36,37] In the design, eumelanin-like PDA with a good photothermal effect is employed to form a conformal layer on BP NSs, which can improve the photothermal conversion efficiency,[38] provide amine anchors for further functionalization,[39] and enhance the stability of BP NSs.[34] Ce6, a commercial photosensitizer with excellent ROS generation ability and NIR fluorescence, is applied for PDT and fluorescence imaging,[7] while TPP is used to target the mitochondria *via* membrane potential.[40] It should be mentioned that the mitochondria, an indispensable organelle responsible for cell respiration, can mediate apoptosis and emerge as a promising pharmacological target in clinical cancer treatment.[41] As expected, the obtained BP@PDA–Ce6&TPP NSs present excellent synergistic therapeutic effects both *in vitro* and *in vivo*, which can target mitochondria because of TPP, produce considerable heat mainly owing to BP@PDA NSs, and generate sufficient ROS due to Ce6.

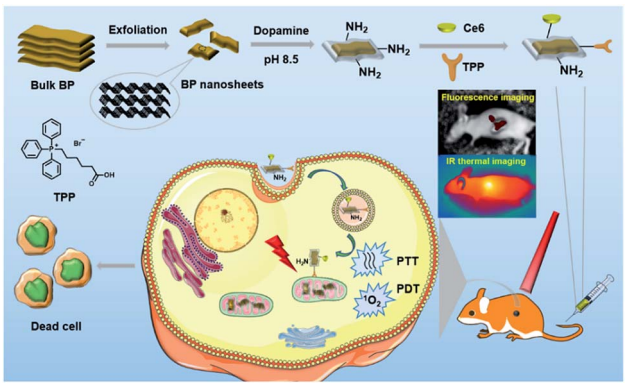

Fig. 1 Schematic illustration of the preparation and therapeutic functions of BP@PDA–Ce6&TPP NSs.

Results and discussion

The X-ray diffraction (XRD) pattern of BP NSs (Fig. S1†) reveals that the BP is an orthorhombic crystal structured NS (JCPDS no. 73-1358).[30,33] Raman spectral analysis (Fig. S2†) shows some characteristic peaks at around 358.7, 435.3, and 465.7 cm^{-1}, corresponding to the typical vibrational modes A_g^1, B_{2g} and A_g^2 of BP, respectively, which is consistent with the reported literature.[30] X-ray photoelectron spectroscopy (XPS) spectra reveal that BP NSs are mainly formed by phosphorus with little oxidation (Fig. S3†).[33]

The morphology of BP NSs before and after PDA coating was characterized by scanning electron microscopy (SEM), transmission electron microscopy (TEM) and atomic force microscopy (AFM). The SEM and TEM images show that BP NSs have a lateral size of around 120 nm (Fig. 2a and b). The AFM images demonstrate that the average thickness of BP NSs is about 24.3 nm (Fig. 2c and d). After coating with PDA, the morphology almost remains intact (Fig. 2e and f), while the height of the NSs increases obviously (~49.1 nm, Fig. 2g and h) due to the BP NS surface modification by PDA. Dynamic light scattering (DLS) analysis shows that the diameter of BP NSs increases from 124.5 nm to 145.3 nm after PDA coating, and then continuously increases to 213.9 nm for the as-prepared BP@PDA–Ce6&TPP NSs (Fig. S5†).

The successful coating of PDA as well as the covalent binding of Ce6 and TPP was further confirmed using UV-vis-NIR absorption spectra, fluorescence spectra and Fourier transform infrared (FT-IR) spectra. BP NSs possess broad absorption without any obvious absorption peaks, while BP@PDA NSs show a new absorption peak at 201 nm, indicating the successful PDA coating (Fig. 2i). Compared with BP@PDA NSs, BP@PDA–Ce6&TPP NSs and BP@PDA–Ce6 NSs exhibit two new absorption peaks at 413/671 and 422/676 nm, respectively, corresponding to the characteristic Soret and Q bands of Ce6 molecules. In addition, a shoulder peak at about 210 nm appears in the spectrum of BP@PDA–Ce6&TPP NSs, which might be caused by the TPP moiety (Fig. 2i). A similar shoulder peak is also observed for BP@PDA–TPP NSs, where only TPP is covalently bound to BP@PDA in the absence of Ce6 (Fig. S7†). Furthermore, the photographs of the aqueous solutions of BP NSs, BP@PDA NSs, BP@PDA–Ce6 NSs, and BP@PDA–Ce6&TPP NSs intuitively demonstrate successful coating by PDA and functionalization by Ce6 (Fig. 2i(I–IV)). In fluorescence spectra, compared with Ce6 (665 nm), BP@PDA–Ce6&TPP NSs show an emission peak at 681 nm with a 16 nm red shift (Fig. 2j). In addition, the fluorescence intensity of BP@PDA–Ce6&TPP NSs is much weaker than that of free Ce6 with an equivalent concentration, which should be due to the overlap of the BP@PDA absorption band and Ce6 emission band. As shown in the FT-IR spectra (Fig. 2k), the characteristic peaks at 3690–3030 and 1632 cm^{-1} for BP@PDA NSs can be assigned to the stretching vibrations of catechol –OH/–NH_2 and C=O, respectively, confirming that PDA was successfully coated onto the surface of BP NSs.[34] After esterification, the two peaks at 3416 and 3127 cm^{-1} change to one, implying the generation of amide. Moreover, a peak at 2927 cm^{-1} occurs, and the peak at

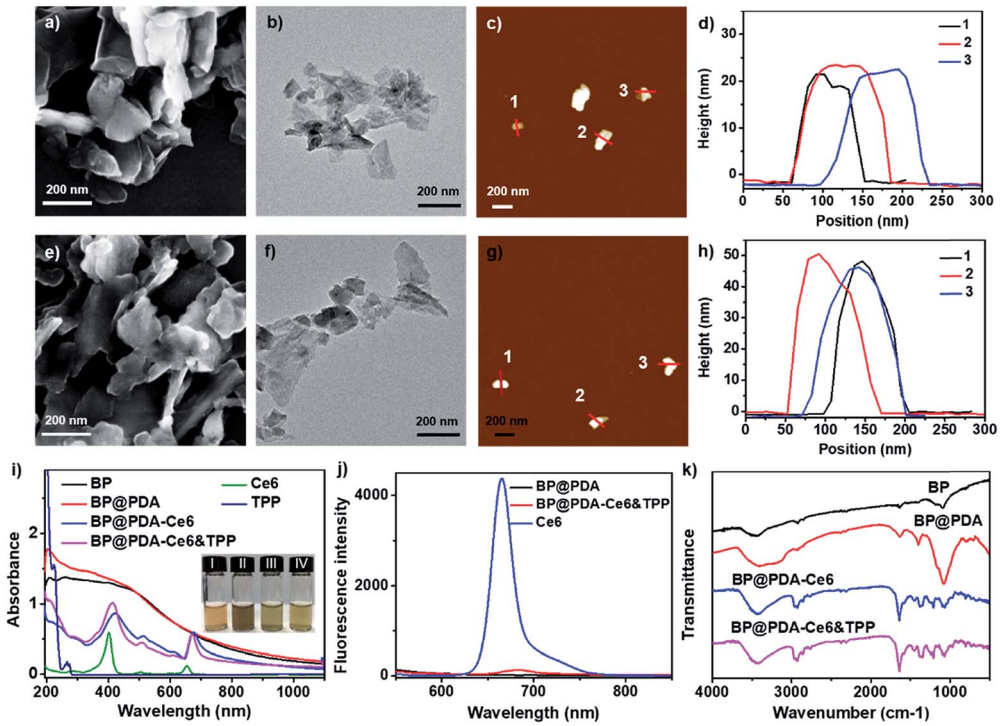

Fig. 2 (a) SEM, (b) TEM, and (c) AFM images and (d) AFM measured thickness of BP NSs. (e) SEM, (f) TEM, and (g) AFM images and (h) AFM measured thickness of BP@PDA NSs. (i) UV-vis-NIR spectra of BP-based nanomaterials. The inset shows the photographs of (I) BP NS, (II) BP@PDA NS, (III) BP@PDA–Ce6 NS, and (IV) BP@PDA–Ce6&TPP NS dispersions. (j) Fluorescence spectra of BP-based nanomaterials. (k) FT-IR spectra of BP-based nanomaterials.

1632 cm^{-1} enhances, which could be attributed to the stretching vibration of alkyl C–H and C=O from Ce6 or TPP. All these results signify the successful PDA coating and the covalent binding of Ce6 as well as TPP.

To prove the potential use of BP@PDA as a photothermal agent, the photothermal performance of the BP@PDA nanosystem was carefully examined with a 660 nm laser. The temperature of BP@PDA NSs rises by 21.9 °C upon irradiation for 10 min, which is much higher than that of BP NSs without PDA coating (14.2 °C, Fig. S9†). Meanwhile, the photothermal conversion efficiency (η) is calculated to be 33.2% and 26.6% for BP@PDA and BP NSs, respectively.[42] All the above results indicate that the PDA coating would optimize the photothermal performance of pure BP NSs. After Ce6 and TPP conjugation, the temperature increment of BP@PDA–Ce6&TPP NSs at different concentrations as well as at different laser power densities was systematically investigated (Fig. 3a and b). The temperature of the BP@PDA–Ce6&TPP NS dispersion quickly rises even at rather low concentrations or low power density of the laser, while pure PBS solution shows little change. Furthermore, the photothermal effect of BP@PDA–Ce6&TPP NSs, BP@PDA–Ce6 NSs and BP@PDA NSs was also studied with the same concentration of BP@PDA or Ce6 (Fig. 3c). There is no significant difference of the temperature elevation of BP@PDA–Ce6&TPP (17.3 °C), BP@PDA–Ce6 (18.3 °C), and BP@PDA (18.6 °C) NSs. Moreover, the temperature of free Ce6 only increases about 6.9 °C, demonstrating that BP@PDA NSs are predominantly responsible for the photothermal conversion, which is consistent with a previous report.[39]

The photodynamic activity of the nanosystem was measured by using 9,10-anthracenediylbis(methylene)dimalonic acid (ABDA) as the indicator (Fig. 3d and S13†).[43] No significant change is observed in the absorbance of ABDA when BP@PDA

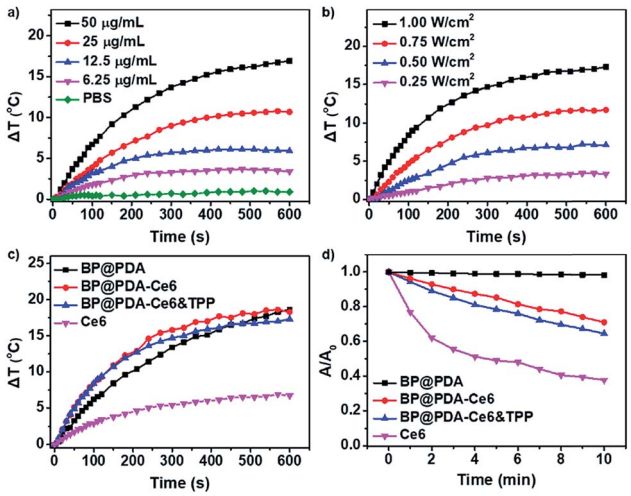

Fig. 3 Photothermal heating profiles of BP@PDA–Ce6&TPP NSs in aqueous solution at (a) different concentrations (660 nm, 1.0 W cm^{-2}, 10 min) and (b) different power densities (50 μg mL^{-1}). (c) Photothermal response of BP@PDA NSs, BP@PDA–Ce6 NSs, BP@PDA–Ce6&TPP NSs, and Ce6 upon laser illumination (660 nm, 1.0 W cm^{-2}, 10 min). (d) The absorbance decay of ABDA at 380 nm in the solutions of BP@PDA NSs, BP@PDA–Ce6 NSs, BP@PDA–Ce6&TPP NSs, and Ce6 upon laser illumination (660 nm, 0.10 W cm^{-2}).

NSs are irradiated with a 660 nm laser (Fig. S13a†).[35] However, remarkable decreases in the absorbance at 380 nm could be observed when both BP@PDA–Ce6 and BP@PDA–Ce6&TPP NSs are exposed to the laser irradiation, indicating the high efficiency ROS generation by Ce6 under 660 nm laser irradiation (Fig. S13b and c†). Furthermore, when Ce6 at an equivalent concentration in PBS is irradiated under the same conditions (Fig. S13d†), the absorbance intensity of ABDA at 380 nm decreases much faster and more ROS are produced compared with BP@PDA–Ce6&TPP NSs, which probably resulted from the partial quenching of Ce6 by BP@PDA NSs. $^1O_2$ generation was also detected by the fluorescent probe singlet oxygen sensor green (SOSG, Fig. S14†).[44] Compared with the control group, the fluorescence intensity of BP@PDA shows a weak change, indicating no $^1O_2$ generation. For the Ce6 group, the fluorescence intensity increases dramatically, demonstrating the excellent $^1O_2$ generation ability of Ce6. While for the BP@PDA–Ce6&TPP NS group, considerable $^1O_2$ was produced after laser irradiation, which could be attributed to the Ce6 photosensitizer. All these results clearly show the excellent photothermal effect and efficient generation of ROS of the as-prepared BP@PDA–Ce6&TPP NSs.

Then HeLa cell uptake of BP@PDA based nanomaterials was studied (Fig. S15†). BP@PDA–Ce6&TPP NS or BP@PDA–Ce6 NS treated HeLa cells show significant red fluorescence, indicating abundant dispersion of the NSs in the cytoplasm. In contrast, the cells cultured with BP@PDA NSs display little fluorescence in the cytoplasm. Subsequently, the mitochondria targeting ability of BP@PDA–Ce6&TPP NSs was investigated by confocal imaging to track Ce6 fluorescence signals. The Hela cells were first incubated with BP@PDA–Ce6&TPP NSs, and then stained with Mito-Tracker Green,[45] a mitochondria-specific staining dye. As shown in Fig. 4a, good overlapping of the fluorescence images from the two channels can be observed for HeLa cells, indicating a selective localization of BP@PDA–Ce6&TPP NSs in mitochondria. While for the control sample BP@PDA–Ce6 NSs without the TPP group, random distribution in cells is observed, and little colocalization effect could be seen (Fig. 4b). The colocalization results signify the presence of TPP in BP@PDA–Ce6&TPP NSs, as well as Ce6. On the other hand, BP@PDA–Ce6&TPP NSs are proved to possess the capability of targeting mitochondria, which could largely promote the efficiency of cancer phototherapy.

Using 2,7′-dichlorodihydrofluorescein diacetate (DCFH-DA) as the intracellular ROS sensor, the photodynamic ability of BP@PDA–Ce6&TPP NSs was measured (Fig. S16†).[46,47] Nonfluorescent DCFH-DA can form green fluorescent 2′,7′-dichlorofluorescein (DCF) upon reacting with ROS and esterase. After 660 nm laser irradiation, little green fluorescence is observed in HeLa cells treated with BP@PDA NSs, indicating the weak intracellular ROS generation ability of BP@PDA NSs. In contrast, BP@PDA–Ce6&TPP NS or BP@PDA–Ce6 NS treated HeLa cells present green fluorescence of DCF in cells after laser irradiation, suggesting ROS generation of both NSs *in vitro*.

Next, *in vitro* phototherapeutic effects of BP@PDA–Ce6&TPP NSs were assessed by 3-(4,5-dimethylthiazol-2-yl)-2,5-diphenyltetrazolium bromide (MTT) assay, calcein AM/PI co-staining assay, and flow cytometry study. No significant decrease in cell viability is found when the cells are incubated with BP@PDA NSs, BP@PDA–Ce6 NSs and BP@PDA–Ce6&TPP NSs without laser illumination, even at a BP@PDA concentration of 25 μg mL^{-1}, indicating the excellent biocompatibility of the three nanoagents (Fig. 4c). After laser illumination (660 nm, 0.5 W cm^{-2}, 5 min), 50% of the BP@PDA–Ce6&TPP NS treated cells are killed, which is much higher than those treated with BP@PDA–Ce6 NSs (32% cell death) and BP@PDA NSs (3% cell death) (BP@PDA concentration of 0.25 μg mL^{-1}, Fig. 4d). With the concentration increasing, the therapeutic efficacy of BP@PDA–Ce6&TPP NSs further increases. At a BP@PDA concentration of 10 μg mL^{-1}, nearly all cells are killed after laser irradiation. However, at the same concentration, more than 5% and 63% of BP@PDA–Ce6 NS and BP@PDA NS treated HeLa cells still survive, respectively. The calcein AM/PI co-staining assay was also used to measure the therapeutic efficacy of these nanoagents, in which the living and dead cells could be marked with green (calcein) and red color (PI-DNA), respectively (Fig. S17b†).[48,49]

The flow cytometry studies also reveal that BP@PDA–Ce6 NSs (Fig. 4g) and BP@PDA–Ce6&TPP NSs (Fig. 4h) exhibit much more effective phototherapeutic effects than BP@PDA NSs (Fig. 4f), which could be due to the photothermal/photodynamic synergistic effect. Meanwhile, the cell death caused by BP@PDA–Ce6 NSs and BP@PDA–Ce6&TPP NSs should be mainly through the late apoptosis mechanism. In addition, BP@PDA–Ce6&TPP NSs show better phototherapeutic effects than BP@PDA–Ce6, which can be attributed to the mitochondria targeting efficacy of the TPP moiety. In general, BP@PDA–Ce6&TPP NSs have the most excellent cancer cell killing ability *in vitro*, indicating the advantages of mitochondria targeting photothermal/photodynamic synergistic cancer therapy.

Considering the intrinsic NIR fluorescence of Ce6 and the high absorbance of BP@PDA, *in vivo* fluorescence and IR thermal imaging were performed to figure out the tumor uptake of the NSs after intravenous injection. At 2 h post-injection, the fluorescence signal from BP@PDA–Ce6&TPP NSs is observed in the tumor region, and the intensity gradually enhances and reaches the maximum at 12 h post-injection, indicating that BP@PDA–Ce6&TPP NSs could gather in the tumor region efficiently *via* the enhanced permeability and retention (EPR) effect (Fig. 5a). This effect is due to the size-dependent uptake of NSs and the lack of a lymphatic system in the tumor tissue.[50] At 24 h post-injection, the fluorescence signal decreases to an extent, indicating that the NSs could be catabolized at the tumor site. Meanwhile, the tumor and major organs were resected. *Ex vivo* fluorescence imaging shows moderate fluorescence in the tumor tissue but much stronger fluorescence in the liver (the potential metabolism process of Ce6), demonstrating the good tumor uptake and effective catabolism of BP@PDA–Ce6&TPP NSs (Fig. 5b). *In vivo* IR thermal imaging was performed at 12 h post-injection of BP@PDA–Ce6&TPP NSs. The temperature of tumor sites increases from around 37.6 to 48.1 °C after 10 min of laser irradiation, which is slightly higher than that of BP@PDA NS accumulated tumors (from around 37.3 to 47.2 °C,

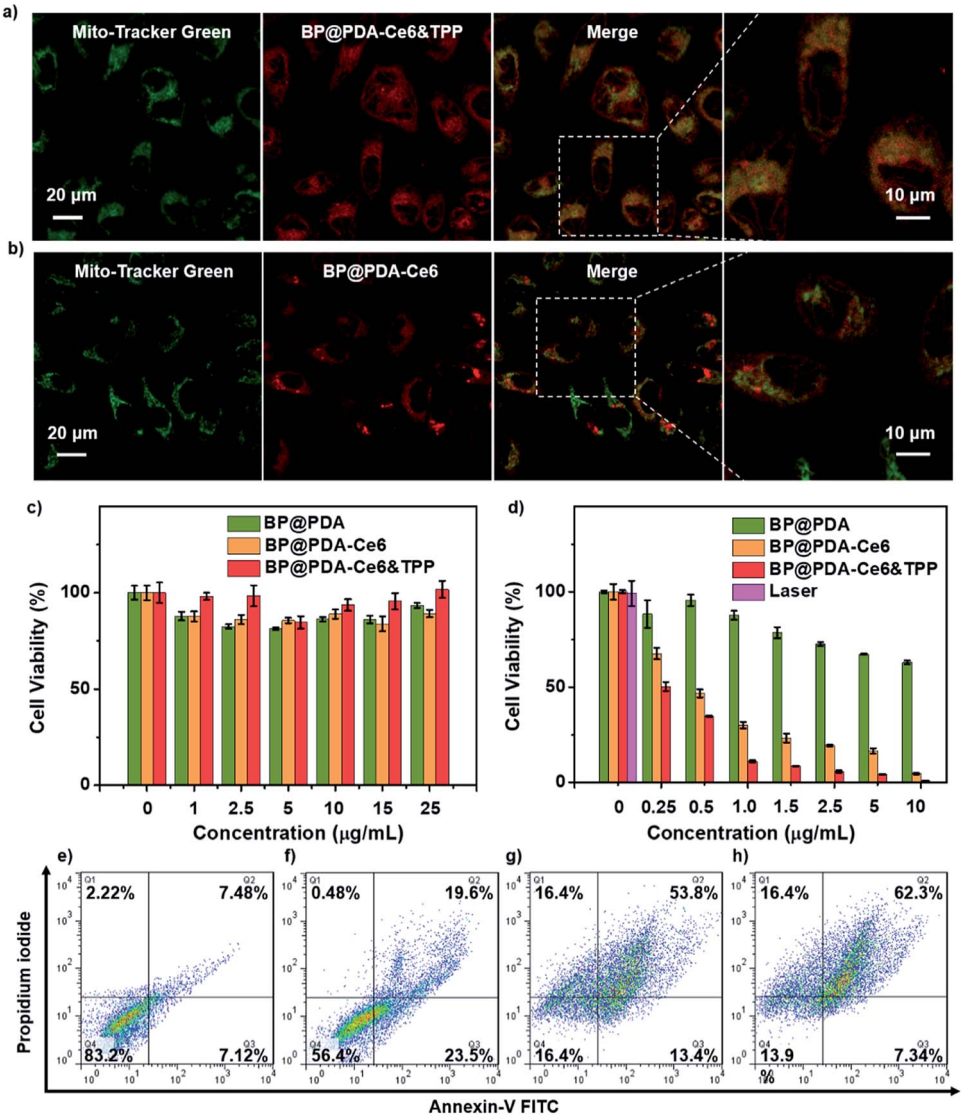

Fig. 4 Confocal fluorescence images of HeLa cells incubated with (a) BP@PDA–Ce6&TPP NSs and (b) BP@PDA–Ce6 NSs (excited at 633 nm) and then Mito-Tracker Green (excited at 488 nm). (c and d) Relative viabilities of HeLa cells incubated with BP@PDA NSs, BP@PDA–Ce6 NSs and BP@PDA–Ce6&TPP NSs at different BP@PDA concentrations (c) without and (d) with laser illumination (660 nm, 0.5 W cm^{-2}, 5 min). Data represent mean ± SD ($n = 4$). (e–h) Flow cytometry studies of HeLa cells incubated (e) without NSs and with (f) BP@PDA NSs, (g) BP@PDA–Ce6 NSs, and (h) BP@PDA–Ce6&TPP NSs at a BP@PDA concentration of 10 μg mL^{-1} with irradiation (660 nm, 0.5 W cm^{-2}, 5 min).

Fig. 5c), whereas the tumor temperature of the PBS injected group only increases from about 37.0 to 40.5 °C within 10 min.

Motivated by the above inspiring results, *in vivo* imaging-guided PDT/PTT was investigated. As mitochondria targeting plays a key role in tumor therapy, *in vivo* therapy was conducted in 5 groups of mice.[51,52] During the treatments, the length and width of tumors were measured every 2 days and the relative tumor volumes (V/V_0) were obtained by normalizing the measured values to the initial sizes. The relative tumor volumes of mice injected with PBS, BP@PDA NSs, or BP@PDA–Ce6&TPP NSs without laser increase quickly during the treatment, revealing little therapeutic effects of the NSs without laser illumination. The growth of tumors could be partly reduced by BP@PDA NS injection with laser irradiation, implying effective tumor growth inhibition due to the PTT of BP@PDA NSs. Inspiringly, for BP@PDA–Ce6&TPP NS injected mice with laser irradiation, the tumors shrink gradually, leaving a black scab, and then are completely cured after 14 days, proving the most excellent tumor ablation effect of BP@PDA–Ce6&TPP NSs, which is ascribed to the mitochondria-targeting synergistic PTT/PDT (Fig. 5d, e and g).

Meanwhile, the potential toxicity of BP@PDA–Ce6&TPP NSs was studied. During the treatment, there is no observed decrease in the body weight of mice (Fig. 5f), showing little side effects and good biocompatibility of the NSs. Moreover, histological evaluation of major organs stained with hematoxylin and eosin (H&E) proves no significant organ damage or inflammatory lesion in all major organs after combined PTT and PDT

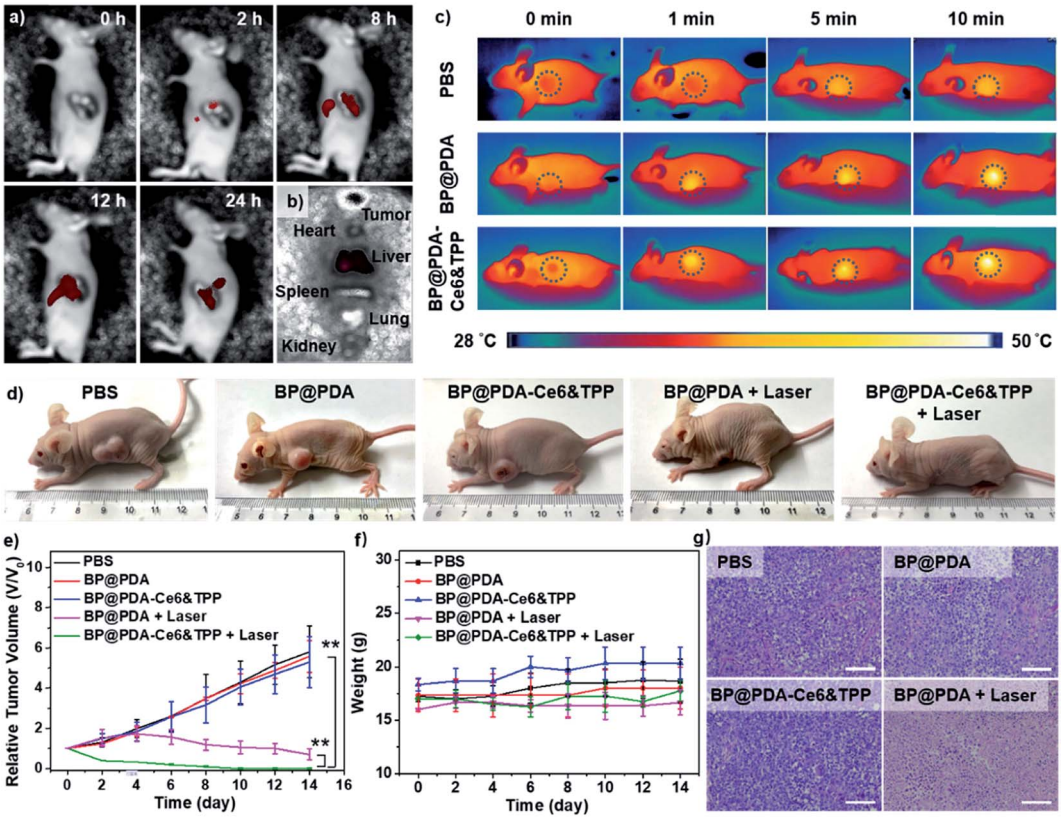

Fig. 5 (a) *In vivo* fluorescence imaging of tumor-bearing mice after BP@PDA–Ce6&TPP NS injection. (b) *Ex vivo* fluorescence imaging of main organs as well as tumor at 24 h post-injection. (c) IR thermal imaging of mice after injection of BP@PDA NSs or BP@PDA–Ce6&TPP NSs under laser illumination for 10 min. (d) Photographs of tumor-bearing mice with different treatments. (e) Relative tumor volumes of mice in different treatments as a function of time ($n = 4$, mean ± SD, $^{**}P < 0.005$). (f) Body weight of mice during treatment. (g) Histological microscopy images of the tumor tissues stained with H&E after different treatments. Scale bar: 100 μm.

treatment (Fig. S18†). Therefore, the as-prepared BP@PDA–Ce6&TPP NSs demonstrate great potential for dual-modal imaging guided synergistic PTT/PDT.

Conclusions

In conclusion, a mitochondria-targeting nanosystem, BP@PDA–Ce6&TPP NSs, has been constructed through covalently incorporating both chlorin e6 (Ce6) and triphenyl phosphonium (TPP) onto BP@PDA NSs for dual-modal imaging-guided synergistic photothermal and photodynamic cancer therapy. Polydopamine (PDA) coated on BP NSs can not only enhance the photothermal conversion efficiency (from 26.6% to 33.2%), but also provide an amine linker for further chemical functionalization. The as-prepared multifunctional BP@PDA–Ce6&TPP NSs can target mitochondria, produce considerable heat mainly owing to BP@PDA NSs, and generate sufficient ROS. This study provides a novel strategy for fabricating effective nanotheranostic systems and should shed light on nanomaterial based phototherapy, offering new insights for cancer therapy.

Conflicts of interest

There are no conflicts to declare.

Acknowledgements

The work was supported by the NNSF of China (61525402, 61728401, 51803091, and 21507059), Jiangsu Provincial Key Research and Development Plan (BE2017741), and Six Talent Peak Innovation Team in Jiangsu Province (TD-SWYY-009). All animal experiments were performed in compliance with National Institutes of Health (NIH) guidelines for the care and use of laboratory animals (NIH Publication no. 85-23 Rev. 1985). Besides, all experiments have been approved by the School of Pharmaceutical Sciences, Nanjing Tech University (Nanjing, China).

References

1 B. Yang, Y. Chen and J. Shi, *Chem*, 2018, **4**, 1284–1313.
2 S. Chakrabortty, B. K. Agrawalla, A. Stumper, N. M. Vegi, S. Fischer, C. Reichardt, M. Kögler, B. Dietzek, M. Feuring-Buske, C. Buske, S. Rau and T. Weil, *J. Am. Chem. Soc.*, 2017, **139**, 2512–2519.
3 X. Song, Q. Chen and Z. Liu, *Nano Res.*, 2014, **8**, 340–354.
4 Y. Chen, L. Wang and J. Shi, *Nano Today*, 2016, **11**, 292–308.
5 H. Shi, W. Sun, C. Liu, G. Gu, B. Ma, W. Si, N. Fu, Q. Zhang, W. Huang and X. Dong, *J. Mater. Chem. B*, 2016, **4**, 113–120.

6 C. Zeng, W. Shang, X. Liang, Q. Chen, C. Chi, Y. Du, C. Fang and J. Tian, *ACS Appl. Mater. Interfaces*, 2016, **8**, 29232–29241.
7 G. Yang, L. Xu, Y. Chao, J. Xu, X. Sun, Y. Wu, R. Peng and Z. Liu, *Nat. Commun.*, 2017, **8**, 902.
8 S. P. Sherlock, S. M. Tabakman, L. Xie and H. Dai, *ACS Nano*, 2011, **5**, 1505–1512.
9 L. Gong, L. Yan, R. Zhou, J. Xie, W. Wu and Z. Gu, *J. Mater. Chem. B*, 2017, **5**, 1873–1895.
10 T. Liu, C. Wang, W. Cui, H. Gong, C. Liang, X. Shi, Z. Li, B. Sun and Z. Liu, *Nanoscale*, 2014, **6**, 11219–11225.
11 P. Liang, Q. Tang, Y. Cai, G. Liu, W. Si, J. Shao, W. Huang, Q. Zhang and X. Dong, *Chem. Sci.*, 2017, **8**, 7457.
12 Q. Tang, W. Si, C. Huang, K. Ding, W. Huang, P. Chen, Q. Zhang and X. Dong, *J. Mater. Chem. B*, 2017, **5**, 1566.
13 J. Zou, P. Wang, Y. Wang, G. Liu, Y. Zhang, Q. Zhang, J. Shao, W. Si, W. Huang and X. Dong, *Chem. Sci.*, 2019, **10**, 268–276.
14 Y. Wang, X. Huang, Y. Tang, J. Zou, P. Wang, Y. Zhang, W. Si, W. Huang and X. Dong, *Chem. Sci.*, 2018, **9**, 8103.
15 Y. Chen and J. Shi, *Adv. Mater.*, 2016, **28**, 3235.
16 S. Su, J. Wang, E. Vargas, J. Wei, R. Martínez-Zaguilán, S. R. Sennoune, M. L. Pantoya, S. Wang, J. Chaudhuri and J. Qiu, *ACS Biomater. Sci. Eng.*, 2016, **2**, 1357–1366.
17 L. Shao, R. Zhang, J. Lu, C. Zhao, X. Deng and Y. Wu, *ACS Appl. Mater. Interfaces*, 2017, **9**, 1226–1236.
18 C. Li, Y. Zhang, Z. Li, E. Mei, J. Lin, F. Li, C. Chen, X. Qing, L. Hou, L. Xiong, H. Hao, Y. Yang and P. Huang, *Adv. Mater.*, 2018, **30**, 1706150.
19 G. Liu, J. Zou, Q. Tang, X. Yang, Y. Zhang, Q. Zhang, W. Huang, P. Chen, J. Shao and X. Dong, *ACS Appl. Mater. Interfaces*, 2017, **9**, 40077–40086.
20 C. Dai, Y. Chen, X. Jing, L. Xiang, D. Yang, H. Lin, Z. Liu, X. Han and R. Wu, *ACS Nano*, 2017, **11**, 12696–12712.
21 Y. Liu, X. Ji, J. Liu, W. W. L. Tong, D. Askhatova and J. Shi, *Adv. Funct. Mater.*, 2017, **27**, 1703261.
22 G. Yang, R. Zhang, C. Liang, H. Zhao, X. Yi, S. Shen, K. Yang, L. Cheng and Z. Liu, *Small*, 2018, **14**, 1702664.
23 T. T. Tran, K. Bray, M. J. Ford, M. Toth and I. Aharonovich, *Nat. Nanotechnol.*, 2016, **11**, 37–41.
24 H. Zhang, Y. H. Li, Y. Chen, M. M. Wang, X. S. Wang and X. B. Yin, *Sci. Rep.*, 2017, **7**, 44153.
25 Y. Dong, Q. Wang, H. Wu, Y. Chen, C. H. Lu, Y. Chi and H. H. Yang, *Small*, 2016, **12**, 5376–5393.
26 X. Qian, Z. Gu and Y. Chen, *Mater. Horiz.*, 2017, **4**, 800–816.
27 X. Yang, G. Liu, Y. Shi, W. Huang, J. Shao and X. Dong, *Nanotechnology*, 2018, **29**, 222001.
28 Z. Sun, H. Xie, S. Tang, X. F. Yu, Z. Guo, J. Shao, H. Zhang, H. Huang, H. Wang and P. K. Chu, *Angew. Chem., Int. Ed.*, 2015, **54**, 11688.
29 J. Shao, H. Xie, H. Huang, Z. Li, Z. Sun, Y. Xu, Q. Xiao, X. F. Yu, Y. Zhao, H. Zhang, H. Wang and P. K. Chu, *Nat. Commun.*, 2016, **7**, 12967–12979.
30 H. Wang, X. Yang, W. Shao, S. Chen, J. Xie, X. Zhang, J. Wang and Y. Xie, *J. Am. Chem. Soc.*, 2015, **137**, 11376–11382.
31 W. Chen, J. Ouyang, H. Liu, M. Chen, K. Zeng, J. Sheng, Z. Liu, Y. Han, L. Wang, J. Li, L. Deng, Y. N. Liu and S. Guo, *Adv. Mater.*, 2017, **29**, 1603864.
32 D. Yang, G. Yang, P. Yang, R. Lv, S. Gai, C. Li, F. He and J. Lin, *Adv. Funct. Mater.*, 2017, **27**, 1700371.
33 W. Tao, X. Zhu, X. Yu, X. Zeng, Q. Xiao, X. Zhang, X. Ji, X. Wang, J. Shi, H. Zhang and L. Mei, *Adv. Mater.*, 2017, **29**, 1603276.
34 X. Zeng, M. Luo, G. Liu, X. Wang, W. Tao, Y. Lin, X. Ji, L. Nie and L. Mei, *Adv. Sci.*, 2018, 1800510.
35 X. Yang, D. Wang, Y. Shi, J. Zou, Q. Zhao, Q. Zhang, W. Huang, J. Shao, X. Xie and X. Dong, *ACS Appl. Mater. Interfaces*, 2018, **10**, 12431–12440.
36 R. Liu, Y. Guo, G. Odusote, F. Qu and R. D. Priestley, *ACS Appl. Mater. Interfaces*, 2013, **5**, 9167–9171.
37 L. S. Lin, Z. X. Cong, J. B. Cao, K. M. Ke, Q. L. Peng, J. Gao, H. H. Yang, G. Liu and X. Chen, *ACS Nano*, 2014, **8**, 3876–3883.
38 Y. Dai, D. Yang, D. Yu, C. Cao, Q. Wang, S. Xie, L. Shen, W. Feng and F. Li, *ACS Appl. Mater. Interfaces*, 2017, **9**, 26674–26683.
39 D. Zhang, M. Wu, Y. Zeng, L. Wu, Q. Wang, X. Han, X. Liu and J. Liu, *ACS Appl. Mater. Interfaces*, 2015, **7**, 8176–8187.
40 D. Chen, J. Zhang, Y. Tang, X. Huang, J. Shao, W. Si, J. Ji, Q. Zhang, W. Huang and X. Dong, *J. Mater. Chem. B*, 2018, **6**, 4522–4530.
41 Z. Zheng, T. Zhang, H. Liu, Y. Chen, R. T. K. Kwok, C. Ma, P. Zhang, H. H. Y. Sung, I. D. Williams, J. W. Y. Lam, K. S. Wong and B. Z. Tang, *ACS Nano*, 2018, **12**, 8145–8159.
42 Q. Tian, F. Jiang, R. Zou, Q. Liu, Z. Chen, M. Zhu, S. Yang, J. L. Wang, J. H. Wang and J. Hu, *ACS Nano*, 2011, **5**, 9761–9771.
43 Y. Cai, Q. Tang, X. Wu, W. Si, Q. Zhang, W. Huang and X. Dong, *ACS Appl. Mater. Interfaces*, 2016, **8**, 10737–10742.
44 W. Xiao, P. Wang, C. Ou, X. Huang, Y. Tang, M. Wu, W. Si, J. Shao, W. Huang and X. Dong, *Biomaterials*, 2018, **183**, 1–9.
45 M. Guo, H. J. Xiang, Y. Wang, Q. L. Zhang, L. An, S. P. Yang, Y. Ma and J. G. Liu, *Chem. Commun.*, 2017, **53**, 3253–3256.
46 Q. Tang, W. Xiao, C. Huang, W. Si, J. Shao, W. Huang, P. Chen, Q. Zhang and X. Dong, *Chem. Mater.*, 2017, **29**, 5216–5224.
47 D. Chen, Q. Tang, J. Zou, X. Yang, W. Huang, Q. Zhang, J. Shao and X. Dong, *Adv. Healthcare Mater.*, 2018, **7**, 1701272.
48 G. Liu, S. Zhang, Y. Shi, X. Huang, Y. Tang, P. Chen, W. Si, W. Huang and X. Dong, *Adv. Funct. Mater.*, 2018, **28**, 1804317.
49 B. Yang, J. Yin, Y. Chen, S. Pan, H. Yao, Y. Gao and J. Shi, *Adv. Mater.*, 2018, **30**, 1705611.
50 H. S. Peng and D. T. Chiu, *Chem. Soc. Rev.*, 2015, **44**, 4699–4722.
51 C. Yue, Y. Yang, C. Zhang, G. Alfranca, S. Cheng, L. Ma, Y. Liu, X. Zhi, J. Ni, W. Jiang, J. Song, J. M. de la Fuente and D. Cui, *Theranostics*, 2016, **6**, 2352–2366.
52 L. Xing, J. Y. Lyu, Y. Yang, P. F. Cui, L. Q. Gu, J. B. Qiao, Y. J. He, T. Q. Zhang, M. Sun, J. J. Lu, X. Xu, Y. Liu and H. L. Jiang, *Chem. Commun.*, 2017, **53**, 8790.